HHS Public Access

Author manuscript

Magn Reson Med. Author manuscript; available in PMC 2020 January 01.

Published in final edited form as:

Magn Reson Med. 2019 January ; 81(1): 167–181. doi:10.1002/mrm.27358.

STimulated Echo based Mapping (STEM) of T1, T2 and Apparent Diffusion Coefficient: Validation and Protocol Optimization

Yuxin Zhang, B.S.[1,2], **Shane A. Wells, M.D.**[2], and **Diego Hernando, Ph.D.**[1,2]

[1]Department of Medical Physics, University of Wisconsin Madison, Madison, WI, United States

[2]Department of Radiology, School of Medicine and Public Health, University of Wisconsin Madison, Madison, WI, United States

Abstract

Purpose—To present a STimulated-Echo based Mapping (STEM) approach for simultaneous T1, T2 and ADC mapping.

Methods—Diffusion-weighted stimulated-echo images with various combinations of mixing time (TM), echo time (TE) and b-value were acquired to enable simultaneous mapping of T1, T2 and ADC. The proposed STEM method was performed by densely-sampling the TM-TE-b space in a phantom and in brain and prostate of healthy volunteers. T1, T2, and ADC from STEM were compared to reference mapping methods. Additionally, protocol optimization was performed to enable rapid STEM acquisition within 2 minutes by sparsely sampling the TM-TE-b space. The T1, T2 and ADC measurements from rapid acquisitions were compared to the densely-sampled STEM for evaluation. Finally, a patient with biopsy-proven high-risk prostate cancer was imaged to demonstrate the ability of STEM to differentiate cancer and healthy tissues.

Results—Relative to the reference measurements, densely-sampled STEM provided accurate quantitative T1, T2 and ADC mapping in phantoms (R^2=0.999, slope between 0.97-1.03), as well as in brain and prostate. Further, the T1, T2 and ADC measurements from the optimized rapid STEM acquisitions agreed closely with densely-sampled STEM. Finally, STEM showed decreased T2 and ADC in prostate cancer compared to healthy prostate tissue.

Discussion—STEM provides accurate simultaneous mapping of T1, T2, and ADC. This method may enable rapid and accurate multi-parametric tissue characterization for clinical and research applications.

Keywords

Stimulated-echo DWI; Multi-parametric mapping; Relaxometry; Quantitative diffusion

INTRODUCTION

Quantitative multi-parametric MRI may enable improved diagnosis and treatment monitoring in multiple clinical applications. For example, quantitative T1 and T2 mapping

*Corresponding author: Diego Hernando, Departments of Radiology and Medical Physics, University of Wisconsin-Madison, Madison, WI 53705 USA, dhernando@wisc.edu.

have potential in the diagnosis of brain (1–2) and cardiac (3–5) diseases. Additionally, quantitative mapping of T1 or T2, together with apparent diffusion coefficient (ADC) has applications in the diagnosis and treatment monitoring of prostate disease (6–8) and breast cancer (9). Mapping of relaxation and diffusion parameters may enable advanced characterization of healthy and diseased tissue, with emerging clinical and research applications (10–15). Further, quantitative MRI methods are promising in order to facilitate comparison of data longitudinally or between centers.

Mapping of relaxation and diffusion parameters is typically performed using multiple separate acquisitions, including one or several relaxometry pulse sequences (16–19) and a separate diffusion-weighted imaging (DWI) sequence (20). However, the need for multiple separate acquisitions is often not practical for clinical applications, due to long acquisition times and the challenges of obtaining co-registered parametric maps. Therefore, simultaneous mapping of relaxation (e.g., T1 and T2) and diffusion (e.g., ADC) parameters based on a single acquisition sequence is highly desirable in order to provide rapid and co-registered quantitative multi-parametric MRI.

Previous studies have explored simultaneous T1, T2 and ADC mapping with methods including diffusion-weighted Dual-Echo Steady State (DESS) (22) and MR Fingerprinting (MRF) (21). However, these previously proposed techniques face substantial limitations. For the DESS method, the signal from steady-state sequence is complicated to model, especially with diffusion encoding, which may result in inaccuracy and large variance in diffusion measurements (22). Although preliminary results have shown promise for MRF with simultaneous ADC mapping (21, 36), probing diffusion within the MRF framework is challenging and may be subject to multiple confounding factors (37).

STimulated-Echo (STE) based simultaneous T1, T2 and ADC mapping is a promising approach to overcome the limitations of previous techniques. The STE diffusion weighted imaging (DWI) pulse sequence enables the modulation of T1, T2 and diffusion weighting by varying the mixing time (TM), echo time (TE) and b-values, respectively. As a result, by acquiring multiple (at least four) STE images with varying TM, TE, and b-values, simultaneous co-registered mapping of T1, T2 and ADC is possible. A previously proposed method has implemented STE together with spin echo (SE) to enable T1 mapping (19). Stimulated-echo acquisition mode (STEAM) (23) has also been widely used for MR Spectroscopy-based relaxometry (41–42) and DWI (43–44). However, the lack of a reliable and efficient simultaneous T1, T2 and ADC mapping technique continues to be an important unmet need.

In this study, a STimulated-Echo based Mapping (STEM) method is proposed for rapid and co-registered simultaneous mapping of T1, T2 and ADC. The feasibility, accuracy, and protocol optimization of STEM are evaluated in diffusion phantoms, brain tissues and prostate tissues of healthy volunteers.

METHODS

STEM Acquisition

The proposed STEM acquisition is based on the STE-DWI sequence (24), as shown in Figure 1. Multiple STE images with various values of TM, TE, and b-values are acquired to obtain different T1, T2 and diffusion contrasts. In this study, TR is fixed for each TM, TE and b-value combination.

Signal Model

In this work, the signal from a STE-DWI acquisition is modeled as four exponential decays, including T1 dependence from repetition time (TR), T1-weighting from TM, T2-weighting from TE and diffusion-weighting from b-value. The acquired STEM signal is modeled as

$$S = A\left(1 - e^{-\frac{TR_{eff}}{T1}}\right)e^{\left(-\frac{TM}{T1}\right)}e^{\left(-\frac{TE}{T2}\right)}e^{(-bADC)}, \quad [1]$$

where

$$TR_{eff} = TR - TM - \frac{TE}{2}. \quad [2]$$

Multiple images with different TM, TE and b-value combinations are used to fit the signal model. In the proposed method, T1 relaxation, T2 relaxation and ADC, as well as proton density weighted maps A, are jointly estimated by voxel-wise non-linear least-squares fitting of Eq.1.

More sophisticated models including non-Gaussian diffusion (15) and multi-compartment models (32, 38, 39) may also be feasible from the STEM acquisitions. However, the scope of this study is restricted to the model in Eq.1 for simplicity.

Validation Experiments

Phantom Validation—A twelve-vial (50mL each) T1/T2/diffusion phantom was constructed by mixing acetone (as a signal source) with various concentrations of DI water (to modulate the ADC of acetone) and $MnCl_2$ (to modulate both T1 and T2 of acetone) (25). Images were acquired at room temperature on a 3T scanner (Discovery MR750, GE Healthcare, Waukesha, WI) with a 32-channel Torso coil (GE Healthcare, Waukesha, WI). The proposed STEM acquisition was obtained with four TM-TE combinations, each with six b-values. Total acquisition time for STEM images was 8 minutes. Additionally, reference T1 (16), T2 and ADC maps were acquired (see details in Table 1). Quantitative T1, T2 and ADC maps were calculated from the STEM images following the signal model described in Equation 1. Measurements were made from each quantitative map using a $1cm^2$ region-of-interest (ROI) within each vial.

Brain Imaging—After IRB approval and informed written consent, healthy volunteers (n=8) were scanned at the 3T scanner with an eight-channel head coil (GE Healthcare, Waukesha, WI) for brain mapping. The STEM acquisitions and reference T1, T2 and ADC mapping sequences were performed in each volunteer with interleaved slices were acquired within a TR (detailed imaging protocol shown in Table 2(a)). A single diffusion direction was used in this early stage study to save acquisition time. Note that the ADC maps from a single STE-DWI acquisition (TE=40ms, TM=100ms) instead of Spin-Echo DWI were used as reference to match the diffusion time of the proposed method under restricted diffusion (48). Histograms of pixel-wise quantitative measurements covering the entire slice were plotted in two different slices. In order to measure T1, T2 and ADC, co-localized ROIs were drawn in the parietal right white matter within the corona radiata (WM, ~1cm^2), as well as in the parietal right gray matter (GM, 40mm^2) for statistical analysis (26). ROIs were drawn in the same region for all volunteers, and the averaged measurements as well as standard deviation across volunteers were calculated.

Prostate Imaging—After IRB approval and informed written consent, healthy volunteers (n=8) were scanned at the same 3T scanner with a 32-channel torso coil for prostate mapping. No antiperistaltic agents were used in this study. As shown in Table 2(b), the STEM acquisitions were performed with eight TE and TM combinations, each with six b-values and a single diffusion direction. Interleaved slices were acquired within a TR. Due to scan time limitations, DESPOT1 (17) was performed as the reference T1 map. Also, similar to brain imaging, a single STE-DWI acquisition (TE=40ms, TM=100ms was used as reference because of restricted diffusion in the prostate (49–51). Histograms of pixel-wise quantitative T1, T2, and ADC measurements within the prostate were evaluated from a single slice covering the mid-gland of the prostate. Co-localized ROIs were drawn in the peripheral zone (PZ, 40mm^2) and central gland (CG, 40mm^2) for further quantitative evaluation of T1, T2, and ADC. ROIs were drawn in the same region for all volunteers, and the averaged measurements as well as standard deviation across volunteers were calculated.

Protocol Optimization for Rapid STEM Acquisition

In the validation experiments described above, relatively dense sampling of the TM-TE-b space was used to validate the feasibility of STEM. However, this dense sampling results in time-consuming acquisitions. Ideally, in order to estimate T1, T2 and ADC from the signal model in Eq.1, it suffices to acquire two different TM, TE and b-values (ie: at least four total images are needed). The choice of TM, TE and b-values can be formulated as an optimization problem. In this work, this protocol optimization problem was formulated as a minimax problem of the Cramér-Rao Lower Bound (CRLB)-based standard deviation of the resulting T1, T2 and ADC estimates. The optimization problem was formulated as follows:

$$\hat{\theta} = \mathrm{argmin}_{\theta \in \mathbf{\Theta}} \max \left\{ \sigma^2 \Big|_{(T1,\, T2,\, ADC) \varepsilon \mathbf{\Omega}} \right\} = \mathrm{argmin}_{\theta \in \mathbf{\Theta}} \max \quad [3]$$

$$\left\{ \left(\frac{\sigma_{T1}}{T1} \right)^2 + \left(\frac{\sigma_{T2}}{T2} \right)^2 + \left(\frac{\sigma_{ADC}}{ADC} \right)^2 \Big|_{(T1,\, T2,\, ADC) \varepsilon \mathbf{\Omega}} \right\}.$$

In this optimization problem, **Ω** is the given T1-T2-ADC space that defines the range of tissue parameters under consideration, and **Θ** is the constraint space determined by the scanner and pulse sequence properties. Additionally, $\hat{\theta}$ is a vector containing the optimized protocol parameters, which in this work are defined as TE_1, TE_2, TM_1, TM_2 and two b-values b_1 and b_2. These acquisition parameters determine the four acquired images with [TE_1, TM_1, b_1], [TE_2, TM_1, b_1] and [TE_1, TM_2, b_1] and [TE_1, TM_1, b_2], respectively. Further, σ_{T1}, σ_{T2} and σ_{ADC} are the standard deviation from CRLB analysis of the magnitude signal with a given SNR (Rician noise) (40). The sum of squares of the relative standard deviations is chosen as the cost function to ensure a balanced consideration of the noise performance of T1, T2 and ADC estimation.

The constraint space **Θ** includes constraints on the sequence timing and the achievable b-values. First, the two echo times should have a lower bound defined by the RF pulse durations T_{90}^1 and T_{90}^2 and EPI readout train length T_{EPI}:

$$TE \geq \max\left\{\frac{T_{90}^1 + T_{90}^2}{2}, \frac{T_{90}^2}{2} + T_{EPI}\right\}. \quad [4]$$

Similarly, the two mixing times should be longer than the second and the third 90° pulse:

$$TM > T_{90}^2. \quad [5]$$

Second, the maximum achievable b-value with the given TE and TM should be larger than both b_1 and b_2, as follows:

$$b \leq (\gamma G_{max}\delta)^2\left(\Delta - \frac{\delta}{3}\right), \quad [6]$$

where γ is the gyromagnetic ratio and G_{max} is the maximum gradient strength of the scanner. Δ is the diffusion time and δ is the duration of diffusion encoding lobe, assuming infinite slew rate to simplify the description. With minimized TE, Δ and δ can be expressed in terms of the remaining pulse sequence timing parameters including TE, TM and RF pulse durations:

$$\delta = \min\left\{\frac{TE - T_{90}^2}{2} - T_{EPI}, \frac{TE - T_{90}^1 - T_{90}^2}{2}\right\} \quad [7]$$

$$\Delta = \delta + T_{90}^2 + TM. \quad [8]$$

In this study, sequence parameter constraints included $G_{max} = 50 \quad mT/m$, $T_{90}^{1} = 12ms$ for water selective excitation pulse, $T_{90}^{2} = 6.5ms$ and $T_{EPI} = 10ms$. SNR in the simulation, which was equal to the proton density weighted signal A divided by the standard deviation, was set as 50. Optimization was run with different T1-T2-ADC space $\boldsymbol{\Omega}$

for healthy brain and healthy prostate tissues respectively, where $T1 \in (700, \quad 1350)ms$, $T2 \in (50, \quad 150)ms$ and $ADC \in (550, \quad 1400) \times 10^{-6} mm^2/s$ for brain and $T1 \in (600, \quad 1500)ms$, $T2 \in (50, \quad 100)ms$ and $ADC \in (800, \quad 1500) \times 10^{-6} mm^2/s$ for prostate.

With this optimization scenario, the optimal combinations of TE, TM and b-values will be obtained. In this study, optimized rapid acquisitions were selected retrospectively by choosing the optimal combination of TE_1, TE_2, TM_1, TM_2, b_1, b_2 from the densely-sampled acquisitions described above for brain and prostate. Data from the resulting rapid acquisitions were re-fitted to the signal model (Eq.1), to obtain T1, T2, and ADC parametric maps. These parametric maps were compared between the rapid acquisition and the densely-sampled acquisition, in order to preliminarily evaluate the feasibility of the rapid STEM acquisition.

Patient Case Study

A 73-year old with biopsy-proven prostate cancer was recruited from an institutional database. Approximately 60 days prior, a clinical prostate MRI and MRI-US guided biopsy were performed confirming prostate cancer. Following IRB approval and written informed consent, STEM imaging was performed. The same protocol from the healthy prostate volunteers was used. In the estimated T1, T2 and ADC maps, ROIs were drawn supervised by a radiologist with expertise in GU imaging on the normal peripheral zone (PZ) as well as biopsy-proven cancers in the left and right PZ fitting the size of the cancer.

Evaluation of B1 Inhomogeneity Effects

T1 mapping methods are often confounded by B1 inhomogeneity effects. To evaluate the effect of imperfect B1 fields on the quantitative STEM measurements, several STEM acquisitions with different actual flip angles were obtained by adjusting the scanner transmit gain. With this setup, the actual STE sequence performed included three α° pulses instead of the idealized three 90 ° pulses. A $NiCl_2$-doped water phantom was scanned at 3T using an eight-channel head coil with default transmit gain. To adjust the actual flip angle, two additional acquisitions were obtained with transmit gains equal to 45% and 135% of the original transmit gain, respectively. STEM was implemented with TM = [25, 100, 100]ms, TE = [50, 42, 80]ms and b-values(#average) = [0(2),100(2),200(2),400(4),800(8)]s/mm^2. Other parameters included TR=3s, slice thickness = 5mm, FOV = 26cm, in-plane resolution = 2mm × 2mm and diffusion direction = R/L. Bloch-Siegert B1 maps (45) were acquired to measure the actual flip angle in different regions within the acquired slice. Two ROIs (~1cm^2) were drawn from each actual flip angle map of the images acquired with different transmit gains (6 ROIs in total).

The corresponding STEM-based T1, T2 and ADC measurements co-localized with the previously described ROIs were used to analyze the relationship between the quantitative measurements and actual flip angle. Linear regression between each quantitative measurement and the actual flip angles was performed to evaluate the effects of B1 inhomogeneity on STEM measurements.

Dependence of T1, T2, and ADC Quantification on Acquisition Parameters

The proposed STEM acquisition, which samples the MR parameter space along multiple relaxometry and diffusion dimensions, may enable more sophisticated multi-parametric tissue characterization beyond the simplified signal model described in Equation 1. For instance, Equation 1 jointly fits all the data without accounting for the potential dependence of T1/T2/ADC on the acquisition parameters. However, this dependence might occur in tissue, eg: due to the presence of partial volume effects or non-Gaussian diffusion. Therefore, the measured T1 or T2 may vary with increasing b-value, and the measured ADC may vary with increasing TE or TM (even for a constant set of b-values). To evaluate this dependence in both brain and prostate data, separate estimation of each quantitative parameter was performed within four groups of acquisition parameters:

1. Fixed TE = 40ms, for each b-value, calculate T1 maps with TM = [100, 500, 800, 1000]ms (to evaluate the effect of b-value on measured T1);
2. Fixed TM=100ms, for each b-value, calculate T2 maps with TE = [40, 50, 80]ms for the brain and TE = [40, 50, 65]ms for the prostate (to evaluate the effect of b-value on measured T2);
3. Fixed TE = 40ms, for each TM, calculate ADC maps with all six b-values (to evaluate the effect of TM on measured ADC);
4. Fixed TM = 100ms, for each TE, calculate ADC maps with all six b-values (to evaluate the effect of TE on measured ADC).

ROI measurements from the same regions described above for brain and prostate scans were performed in the corresponding maps from each group of parameters, and displayed using box-plots. A Linear Mixed-Effect (LME) fitting model (46) was applied to evaluate the association between measurements and acquisition parameters.

RESULTS

Validation Experiments

Phantom validation: Figure 2 shows T1, T2, and ADC mapping results in the phantom. STEM results in quantitative maps with high image quality and good SNR, although EPI related distortion artifacts remain. Further, these results show excellent quantitative agreement between STEM and the reference T1, T2, and ADC mapping techniques. The R^2 for T1, T2 and ADC are all nearly 0.999. The slope for each parameter is 1.01 ±0.01, 1.03 ± 0.01 and 0.97 ±0.01, respectively. The intercept for each parameter is 1.94 ±2.31ms, −2.51 ±1.5ms and 0.04 ±0.01 $\times 10^{-3}$mm^2/s respectively.

Brain imaging: Representative quantitative maps for two different slices in the brain of a healthy volunteer, with histograms from each entire slice are presented in Figure 3. Orange bars in the histograms are from the reference maps, blue bars are from the STEM maps and red-colored areas are the overlap between the proposed and reference methods. The high overlap between STEM and reference measurement histograms illustrates the accuracy of the proposed STEM method. Nevertheless, the STE-DWI sequence used in STEM has limited spatial resolution compared to the reference IR-FSE T1 mapping and SE T2 mapping techniques.

Prostate imaging: Figure 4 shows representative maps and histograms of the prostate. Although high overall agreement is observed between STEM and the reference mapping methods, some estimation bias and image artifacts may be present in STEM, especially near the edges of the prostate.

Table 3 summarizes the T1, T2, and ADC measurements in the brain and prostate across all subjects. Overall, STEM measurements are in excellent agreement with reference measurements, with similar standard deviation across subjects.

Protocol Optimization for Rapid STEM Acquisition

In the protocol optimization simulations, the optimized acquisition parameters for rapid STEM imaging are TE_1=39.4ms, TE_2=92.2ms, TM_1=123.1ms, TM_2=1026.2ms and b_1=0 s/mm^2 and b_2=826.5 s/mm^2 in the brain and TE_1=39.6ms, TE_2=95.0ms, TM_1=124.2ms, TM_2=1244.5ms and b_1=0 s/mm^2 and b_2=863.9 s/mm^2 in the prostate. Among the parameters acquired in the previously obtained densely-sampled *in-vivo* datasets, the optimal combinations are TE_1=40ms, TE_2=80ms, TM_1=100ms, TM_2=1000ms and b_1=50s/mm^2 and b_2=800s/mm^2 in the brain and TE_1=40ms, TE_2=65ms, TM_1=100ms, TM_2=1000ms and b_1=50s/mm^2 and b_2=800s/mm^2 in the prostate. The optimized rapid STEM acquisitions are less than 2 minutes for both brain and prostate imaging.

Figure S1 shows an example plot of the cost function σ^2 (ie: the sum-of-squares of relative standard deviation for T1-T2-ADC estimation, as a function of the acquisition parameters) used for optimization of rapid acquisition protocols. Figure 5 shows the T1, T2 and ADC maps estimated from the resulting optimized rapid protocol (Figure 5a: brain, Figure 5b: prostate). Quantitative maps from the rapid STEM acquisition are noisier than the original densely-sampled maps; however, the measurements remain accurate. ROI measurements from the rapid STEM acquisitions in brain and prostate are also summarized in Table 3.

Patient Case Study

The patient presented with an elevated PSA of 13.93ng/ml. At MRI, there were 2 suspicious lesions in the prostate including a prostate imaging reporting and data system (PI-RADS) 4 lesion in the left PZ and PI-RADS 5 lesion in the right PZ. Figure 6 shows a representative DWI (b=800s/mm^2), T2-weighted image and the estimated T1, T2 and ADC maps. ROI measurements in the two lesions and the normal prostate tissue are also listed in Figure 6. Both the left and right lesions have lower ADC and T2 values compared to the healthy PZ. The T2 and ADC values with densely-sampled STEM in the lesions are 45.1ms and 810.0

$\times 10^{-6}$mm^2/s for the left lesion and 53.4ms and 1065.3×10^{-6}mm^2/s for the right lesion. For healthy PZ tissue, T2 is 73.1ms and ADC is 1671.3×10^{-6}mm^2/s.

Evaluation of B1 Imperfection

The measured flip angles over the six ROIs in the three acquisitions were 49.1 °, 62.9 °, 100.8 °, 132.4 °, 138.4 ° and 157.6 °, respectively. Based on linear regression analysis, the coefficients (slopes) between T1 and flip angle, T2 and flip angle and ADC and flip angle are -1.23×10^{-2} (P=0.210), 3.90×10^{-3}(P=0.645) and 1.36×10^{-1}(P=0.181), respectively. With a 95% confidence level, quantitative T1, T2 and ADC measurements from STEM acquisitions are not affected by imperfect flip angle.

Dependence of T1, T2, and ADC Quantification on Acquisition Parameters

Box-plots from ROI measurements in the quantitative measurements for varying acquisition parameters are shown in Figure 7. The LME analysis results, including the slope and P-values, are shown in each box-plot. Though the number of volunteers is limited, some measurements are significantly dependent on acquisition parameters. For example, the measured T2 values show a significant decrease with increasing b-values for gray matter as well as for the prostate PZ and CG (P<0.001).

DISCUSSION

In this study, a Stimulated-Echo based Mapping (STEM) method has been proposed for simultaneous quantitative T1, T2 and ADC mapping. The overall T1, T2 and ADC measurements have been shown to be accurate in phantom experiments, brain and prostate imaging. Further, protocol optimization was performed to achieve accurate STEM quantification within 2 minutes. The proposed STEM method may enable rapid and co-registered multi-parametric imaging, with potential clinical applications in the brain, prostate, and breast, among others (1–15).

In brain mapping, the estimated T1 and T2 with densely-sampled STEM and rapid STEM acquisitions are in good agreement with measurements from previous studies (17–18, 21–22, 26–27, 37). The T1 histograms from STEM showed two peaks, representing white matter and gray matter respectively. This is in good agreement with previous T1 mapping studies performed with moderate spatial resolution (16). However, the two peaks are not obvious in the reference T1 map. This may be due to the higher resolution in the reference T1 map, where the different T1 values from CSF and gray matter result in higher spread of T1. Further, measurements from CSF are not shown in this study because the measurements from our reference T1 and T2 mapping method failed in some volunteers likely due to the flow of CSF. However, STEM may suffer the same motion problem in the CSF. Also, the acquisitions in this study are not optimized for very high T1 and T2 measurements. The ADC values measured in this brain fall into the range of literature (26, 28, 37); however, with only one diffusion direction measured in this study, ADC measurements in the white matter (where diffusion is highly anisotropic) are not comparable to the literature.

In healthy prostate mapping, the overall measurements are in generally good agreement with the literature (29–31). However, the ADC values are slightly lower compared to previous spin echo based ADC measurements in healthy prostate tissues (30–31, 47). This discrepancy may be due to the restricted diffusion in the prostate (50–51), which makes ADC measurements dependent on specific acquisition parameters (eg: diffusion time). Also, previous measurements of T1, T2 and ADC have a broad variation across studies (29–31, 47, 49–51), and prostate ADC has been shown to increase with age (47). In the prostate cancer case study, we observed a substantial decrease in the T2 and ADC values within the two lesions relative to healthy peripheral zone tissue, in agreement with the literature (7).

In this study, a simple signal model is used for jointly estimating T1, T2 and ADC values. However, in the presence of restricted diffusion, ADC will generally depend on the acquisition parameters, including choice of b-values and diffusion time. Therefore, more sophisticated diffusion models may be preferable. Also, partial volume effects may arise when multiple tissue components, epithelial and stromal components in the prostate for example, are contained in a voxel. These tissue components generally have different T1, T2 and diffusion properties, which may explain in part the slight underestimation in the *in-vivo* T2 measurements of both brain and prostate compared to the reference SE T2 mapping. These confounding factors, which present a challenge for naïve signal modeling approaches, may also present an opportunity for advanced multi-compartment tissue characterization (32–33) by exploiting the multiple signal dimensions (T1, T2, diffusion) probed by the STEM approach.

In this work, STEM scan times ranged from 1min13s with rapid acquisition to 22min56s with dense sampling of the TM-TE-b space. The acquisition time depends on multiple parameters, including the number of b-values and diffusion directions, and the choice of TM and TE combinations. In principle, a minimum of four images with different TM, TE and b-values are required for STEM. With protocol optimization, the maximum acquired TM and TE should be of the same order as the tissue T1 and T2, respectively. When T1 is very long (over 1000ms, as is the case in the prostate), a long TM (eg: 800-1200ms) would be needed to create enough T1 decay. However, this will result in longer acquisitions with substantial ‘dead time’ during the mixing time. Future work may explore the possibility of increasing the duty cycle by exciting other slices or bands during the mixing time.

Although the proposed STEM approach is promising for accurate quantitative mapping, the current method has several limitations. STEM acquisitions are based on an EPI readout; therefore, they have the same geometric distortions as SE-DWI sequences in areas of B0 field inhomogeneity. More advanced acquisition techniques like reduced FOV (34) and multi-shot EPI (35) may enable reduced distortion in STEM. Also, due to the stimulated echo acquisition, the SNR of STE-DW images is only half the SNR of SE-DW images. Similar to other quantitative techniques, STEM is sensitive to motion during the acquisition. Although each individually acquired STEM image is highly robust to motion due to the single-shot EPI readout, motion between images may introduce artifacts in quantitative maps, particularly near tissue interfaces. For example, in the prostate maps, motion-induced misregistration introduces inaccuracy in T2 and T1 maps. Particularly when using rapid STEM acquisitions, the estimation will be sensitive to artifacts and noise in the images. In

clinical prostate imaging applications, antiperistaltic agents may be used to reduce small bowel motility, which may significantly reduce the artifacts in prostate measurements. For other organs, registration-based approaches may mitigate motion-related artifacts.

In addition, the validation experiments in this paper have several limitations. The quantitative phantom only has a maximum T1 of about 300ms, which is lower than most tissues. To further validate STEM in the presence of long T1 and long T2 measurements, an agar phantom experiment was conducted and shown in supporting information Figure S2. Also in the *in-vivo* mapping experiment, only one diffusion direction was acquired because of the long acquisition time with densely-sampled STEM. Additionally, the rapid acquisitions were performed retrospectively (ie: with a long temporal footprint), leading to increased motion artifacts in prostate mapping. For preliminary assessment of rapid STEM acquisitions with a short temporal footprint, prospective rapid STEM acquisitions were acquired in one brain volunteer and one prostate volunteer in three orthogonal diffusion directions, with the results shown in supporting information Figures S3 and S4. Further, STE-DWI instead of SE-DWI was used as a reference for ADC in this study because ADC will be different for different diffusion time in the presence of non-Gaussian diffusion (48–51). Extensions of this work may include more sophisticated models beyond simple ADC, in order to account for the presence of restricted diffusion.

Finally, this work performed technical validation and optimization of the proposed STEM method, focused largely on quantitative phantoms and healthy volunteers. Although this technical validation is critical for quantitative techniques, clinical validation studies are needed to evaluate the performance of the proposed technique in patients, including patients with prostate cancer and brain disease. While these clinical studies are outside of the scope of this manuscript, we nevertheless included a single clinical example, primarily for illustration purposes.

In summary, we have presented a stimulated-echo based approach termed STEM for simultaneous multi-parametric relaxometry and diffusion mapping. This method provides accurate quantitative maps of T1, T2, and ADC in phantom, brain, and prostate imaging. Further, the proposed approach may enable advanced multi-compartment tissue characterization in multiple parametric dimensions.

Supplementary Material

Refer to Web version on PubMed Central for supplementary material.

Acknowledgments

The authors acknowledge grant support from NIH-NIDDK Wisconsin Multidisciplinary K12 Urologic Research Career Development Program K12DK100022 (PD: D. Bjorling). We also acknowledge research support from GE Healthcare. The authors would like to thank Valentina Taviani, PhD, and Haonan Wang, PhD from GE Healthcare for technical assistance with sequence development. We also thank Xiaoke Wang for assistance with phantom design.

References

1. Neema M, Stankiewicz J, Arora A, Dandamudi VS, Batt CE, Guss ZD, Al-Sabbagh A, Bakshi R. T1-and T2-Based MRI Measures of Diffuse Gray Matter and White Matter Damage in Patients with Multiple Sclerosis. J Neuroimaging. 2007; 17(s):16s–21s. [PubMed: 17425729]
2. Vymazal J, Righini A, Brooks RA, Canesi M, Mariani C, Leonardi M, Pezzoli G. T1 and T2 in the brain of healthy subjects, patients with Parkinson disease, and patients with multiple system atrophy: relation to iron content. Radiology. 1999; 211(2):489–495. [PubMed: 10228533]
3. Bohnen S, Radunski UK, Lund GK, Kandolf R, Stehning C, Schnackenburg B, Adam G, Blankenberg S, Muellerleile K. Performance of T1 and T2 mapping cardiovascular magnetic resonance to detect active myocarditis in patients with recent-onset heart failure. Circ Cardiovascular Imaging. 2015; 8(6):e003070.
4. Blume U, Lockie T, Stehning C, Sinclair S, Uribe S, Razavi R, Schaeffter T. Interleaved T1 and T2 relaxation time mapping for cardiac applications. J Magn Reson Imag. 2009; 29(2):480–487.
5. Kershaw LE, Hutchinson CE, Buckley DL. Benign prostatic hyperplasia: Evaluation of T1, T2, and microvascular characteristics with T1-weighted dynamic contrast-enhanced MRI. J Magn Reson Imag. 2009; 29(3):641–648.
6. Foltz WD, Wu A, Chung P, et al. Changes in apparent diffusion coefficient and T2 relaxation during radiotherapy for prostate cancer. J Magn Reson Imag. 2013; 37(4):909–916. 2013.
7. Gibbs P, Tozer DJ, Liney GP, Turnbull LW. Comparison of quantitative T2 mapping and diffusion-weighted imaging in the normal and pathologic prostate. Magn Reson Med. 2001; 46(6):1054–1058. [PubMed: 11746568]
8. Langer DL, van der Kwast TH, Evans AJ, Trachtenberg J, Wilson BC, Haider MA. Prostate cancer detection with multi-parametric MRI: Logistic regression analysis of quantitative T2, diffusion-weighted imaging, and dynamic contrast-enhanced MRI. J Magn Reson Imag. 2009; 30(2):327–334.
9. Yankeelov TE, Lepage M, Chakravarthy A, et al. Integration of quantitative DCE-MRI and ADC mapping to monitor treatment response in human breast cancer: initial results. Magn Reson Imag. 2007; 25(1):1–13.
10. Li K, Dortch RD, Welch EB, Bryant ND, Buck AK, Towse TF, Gochberg DF, Does MD, Damon BM, Park JH. Multi-parametric MRI characterization of healthy human thigh muscles at 3.0T-relaxation, magnetization transfer, fat/water, and diffusion tensor imaging. NMR Biomed. 2014; 27(9):1070–1084. [PubMed: 25066274]
11. Saab G, Thompson RT, Marsh GD. Multicomponent T2 relaxation of *in-vivo* skeletal muscle. Magn Reson Med. 1999; 42(1):150–157. [PubMed: 10398961]
12. Morvan D, Leroy-Willig A. Simultaneous measurements of diffusion and transverse relaxation in exercising skeletal muscle. Magn Reson Imag. 1995; 13(7):943–948.
13. Tuch DS. Q-ball imaging. Magn Reson Med. 2004; 52(6):1358–1372. [PubMed: 15562495]
14. Yeh FC, Liu L, Hitchens TK, Wu YL. Mapping immune cell infiltration using restricted diffusion MRI. Magn Reson Med. 2017; 77(2):603–612. [PubMed: 26843524]
15. Lu H, Jensen JH, Ramani A, Helpern JA. Three-dimensional characterization of non-Gaussian water diffusion in humans using diffusion kurtosis imaging. NMR Biomed. 2006; 19(2):236–247. [PubMed: 16521095]
16. Barral JK, Gudmundson E, Stikov N, Etezadi-Amoli M, Stoica P, Nishimura DG. A robust methodology for in vivo T1 mapping. Magn Reson Med. 2010; 64(4):1057–1067. [PubMed: 20564597]
17. Deoni SC, Peters TM, Rutt BK. High-resolution T1 and T2 mapping of the brain in a clinically acceptable time with DESPOT1 and DESPOT2. Magn Reson Med. 2005; 53(1):237–241. [PubMed: 15690526]
18. Deoni SC, Rutt BK, Peters TM. Rapid combined T1 and T2 mapping using gradient recalled acquisition in the steady state. Magn Reson Med. 2003; 49(3):515–526. [PubMed: 12594755]
19. Shi X, Kim SE, Jeong EK. Single-shot T1 mapping using simultaneous acquisitions of spin-and stimulated-echo-planar imaging (2D ss-SESTEPI). Magn Reson Med. 2010; 64(3):734–742. [PubMed: 20564579]

20. Bammer R. Basic principles of diffusion-weighted imaging. Eur J Radiol. 2003; 45(3):169–184. [PubMed: 12595101]
21. Jiang Y, Ma D, Wright K, Seiberlich N, Gulani V, Griswold MA. Proceedings of the 23rd Annual Meeting of ISMRM. Milan, Italy: 2014. Simultaneous T1, T2, diffusion and proton density quantification with MR fingerprinting; 0028
22. Gras V, Farrher E, Grinberg F, Shah NJ. Diffusion-weighted DESS protocol optimization for simultaneous mapping of the mean diffusivity, proton density and relaxation times at 3 Tesla. Magn Reson Med. 2017; 78(1):130–141. [PubMed: 27476684]
23. Moonen CT, Kienlin MV, Van Zijl P, Cohen J, Gillen J, Daly P, Wolf G. Comparison of single-shot localization methods (STEAM and PRESS) for In vivo proton NMR spectroscopy. NMR Biomed. 1989; 2(5–6):201–208. [PubMed: 2641894]
24. Merboldt KD, Hänicke W, Frahm J. Diffusion imaging using stimulated echoes. Magnetic Resonance in Medicine. 1991; 19(2):233–239. [PubMed: 1881309]
25. Wang X, Reeder SB, Hernando D. An acetone-based phantom for quantitative diffusion MRI. J Magn Reson Imag. 2017; doi: 10.1002/jmri.25727
26. Helenius J, Soinne L, Perkiö J, et al. Diffusion-weighted MR imaging in normal human brains in various age groups. Am J Radiol. 2002; 23(2):194–199.
27. Kumar R, Delshad S, Woo MA, Macey PM, Harper RM. Age-related regional brain T2-relaxation changes in healthy adults. J Magn Reson Imag. 2012; 35(2):300–308.
28. Clark CA, Hedehus M, Moseley ME. Diffusion time dependence of the apparent diffusion tensor in healthy human brain and white matter disease. Magn Reson Med. 2001; 45(6):1126–1129. [PubMed: 11378893]
29. De Bazelaire CM, Duhamel GD, Rofsky NM, Alsop DC. MR imaging relaxation times of abdominal and pelvic tissues measured in vivo at 3.0 T: preliminary results. Radiology. 2004; 230(3):652–659. [PubMed: 14990831]
30. Medved M, Sammet S, Yousuf A, Oto A. MR imaging of the prostate and adjacent anatomic structures before, during, and after ejaculation: qualitative and quantitative evaluation. Radiology. 2014; 271:452–460. [PubMed: 24495265]
31. Gibbs P, Pickles MD, Turnbull LW. Diffusion imaging of the prostate at 3.0 Tesla. Invest Radiol. 2006; 41:185–188. [PubMed: 16428991]
32. Kim D, Doyle EK, Wisnowski JL, Kim JH, Haldar JP. Diffusion-relaxation correlation spectroscopic imaging: A multidimensional approach for probing microstructure. Magn Reson Med. 2017; doi: 10.1002/mrm.26629
33. Benjamini D, Basser PJ. Use of marginal distributions constrained optimization (MADCO) for accelerated 2D MRI relaxometry and diffusometry. J Magn Reson. 2016; 271:40–45. [PubMed: 27543810]
34. Korn N, Kurhanewicz J, Banerjee S, Starobinets O, Saritas E, Noworolski S. Reduced-FOV excitation decreases susceptibility artifact in diffusion-weighted MRI with endorectal coil for prostate cancer detection. Magn Reson Imag. 2015; 33(1):56–62.
35. Nan-kuei C, Arnaud G, Hing-Chiu C, Song AW. A robust multi-shot scan strategy for high-resolution diffusion weighted MRI enabled by multiplexed sensitivity-encoding (MUSE). NeuroImage. 2013; 72:41–47. [PubMed: 23370063]
36. Yu AC, Badve C, Ponsky LE, et al. Development of a Combined MR Fingerprinting and Diffusion Examination for Prostate Cancer. Radiology. 2017; 283(3):729–738. [PubMed: 28187264]
37. Ma D, Coppo S, Chen Y, McGivney DF, Jiang Y, Pahwa S, Gulani V, Griswold MA. Slice profile and B1 corrections in 2D magnetic resonance fingerprinting. Magn Reson Med. 2017; 78(5):1781–1789. [PubMed: 28074530]
38. Mulkern RV, Zengingonul HP, Robertson RL, et al. Multi-component apparent diffusion coefficients in human brain: relationship to spin-lattice relaxation. Magn Reson Med. 2000; 44(2): 292–300. [PubMed: 10918329]
39. Le Bihan D, Breton E, Lallemand D, Aubin ML, Vignaud J, Laval-Jeantet M. Separation of diffusion and perfusion in intravoxel incoherent motion MR imaging. Radiology. 1988; 168(2): 497–505. [PubMed: 3393671]

40. Karlsen OT, Verhagen R, Bovee WM. Parameter estimation from Rician-distributed data sets using a maximum likelihood estimator: application to T1 and perfusion measurements. Magn Reson Med. 1999; 41:614–623. [PubMed: 10204887]
41. Ruschke S, Kienberger H, Baum T, Kooijman H, Settles M, Haase A, Rychlik M, Rummeny EJ, Karampinos DC. Diffusion-weighted stimulated echo acquisition mode (DW-STEAM) MR spectroscopy to measure fat unsaturation in regions with low proton-density fat fraction. Magn Reson Med. 2016; 75(1):32–41. [PubMed: 25753506]
42. Hamilton G, Middleton MS, Hooker JC, Haufe WM, Forbang NI, Allison MA, Loomba R, Sirlin CB. In vivo breath-hold 1H MRS simultaneous estimation of liver proton density fat fraction, and T1 and T2 of water and fat, with a multi-TR, multi-TE sequence. J Magn Reson Imag. 2015; 42(6):1538–1543.
43. Teruel JR, Cho GY, Moccaldi RT, Goa PE, Bathen TF, Feiweier T, KIM SG, Moy L, Sigmund EE. Stimulated echo diffusion tensor imaging (STEAM-DTI) with varying diffusion times as a probe of breast tissue. J Magn Reson Imag. 2017; 45(1):84–93.
44. Zhang H, Sun A, Li H, Saiviroonporn P, Wu EX, Guo H. Stimulated echo diffusion weighted imaging of the liver at 3 Tesla. Magn Reson Med. 2017; 77(1):300–309. [PubMed: 26877239]
45. Sacolick LI, Wiesinger F, Hancu I, Vogel MW. B1 mapping by Bloch-Siegert shift. Magn Reson Med. 2010; 63(5):1315–1322. [PubMed: 20432302]
46. West BT, Welch KB, Galecki AT. Linear mixed models: a practical guide using statistical software. CRC Press; 2014.
47. Tamada T, Sone T, Toshimitsu S, et al. Age-related and zonal anatomical changes of apparent diffusion coefficient values in normal human prostatic tissues. J Magn Reson Med. 2008; 27:552–556.
48. Panagiotaki E, Schneider T, Siow B, Hall MG, Lythgoe MF, Alexander DC. Compartment models of the diffusion MR signal in brain white matter: a taxonomy and comparison. NeuroImage. 2012; 59:2241–2254. [PubMed: 22001791]
49. Panagiotaki E, Chan RW, Dikaios N, et al. Microstructural characterization of normal and malignant human prostate tissue with vasvular, extracellular and restricted diffusion for cytometry in tumours magnetic resonance imaging. Invest Radio. 2015; 50(4):218–227.
50. Hall MG, Bongers A, Sved P, Watson G, Bourne TM. Assessment of non-Gaussian diffusion with singly and doubly stretched biexponential models of diffusion-weighted MRI (DWI) signal attenuation in prostate tissue. NMR Biomed. 2015; 28:486–495. [PubMed: 25802213]
51. Lemberskiy G, Rosenkrantz AB, Veraart J, Taneja SS, Novikov DS, Fieremans E. Time-dependent diffusion in prostate cancer. Invest Radio. 2017; 52:405–411.

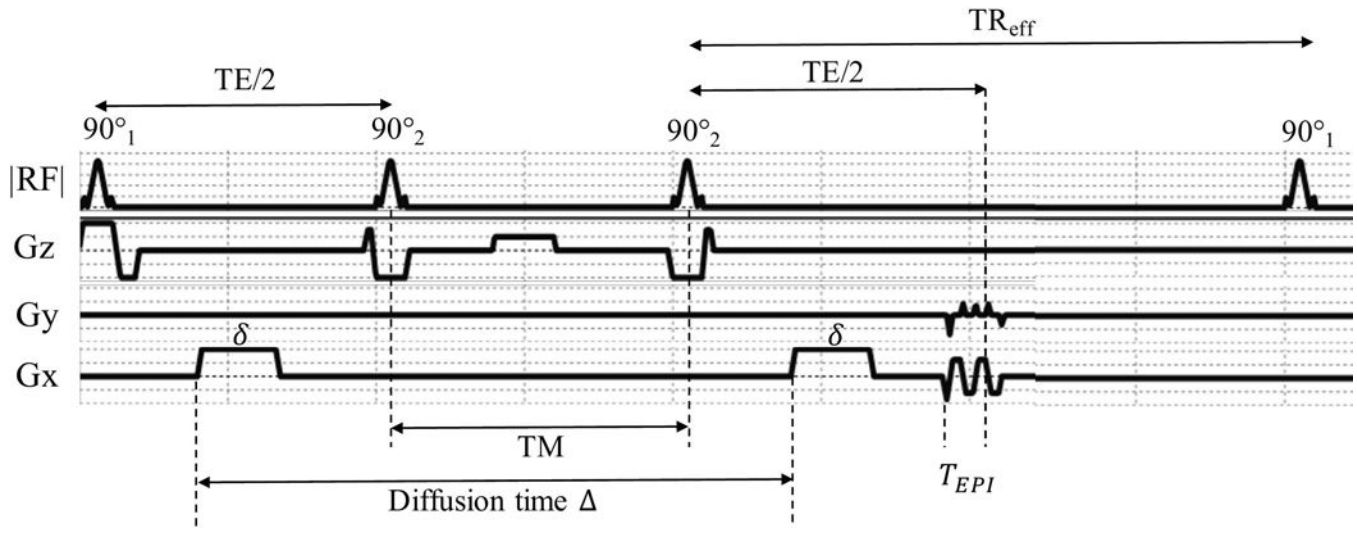

Figure 1.

Sequence profile and timing of stimulated-echo (STE) DWI, where δ is the duration of each diffusion lobe, Δ is the diffusion time and T_{EPI} is the time between the start of EPI readout to TE.

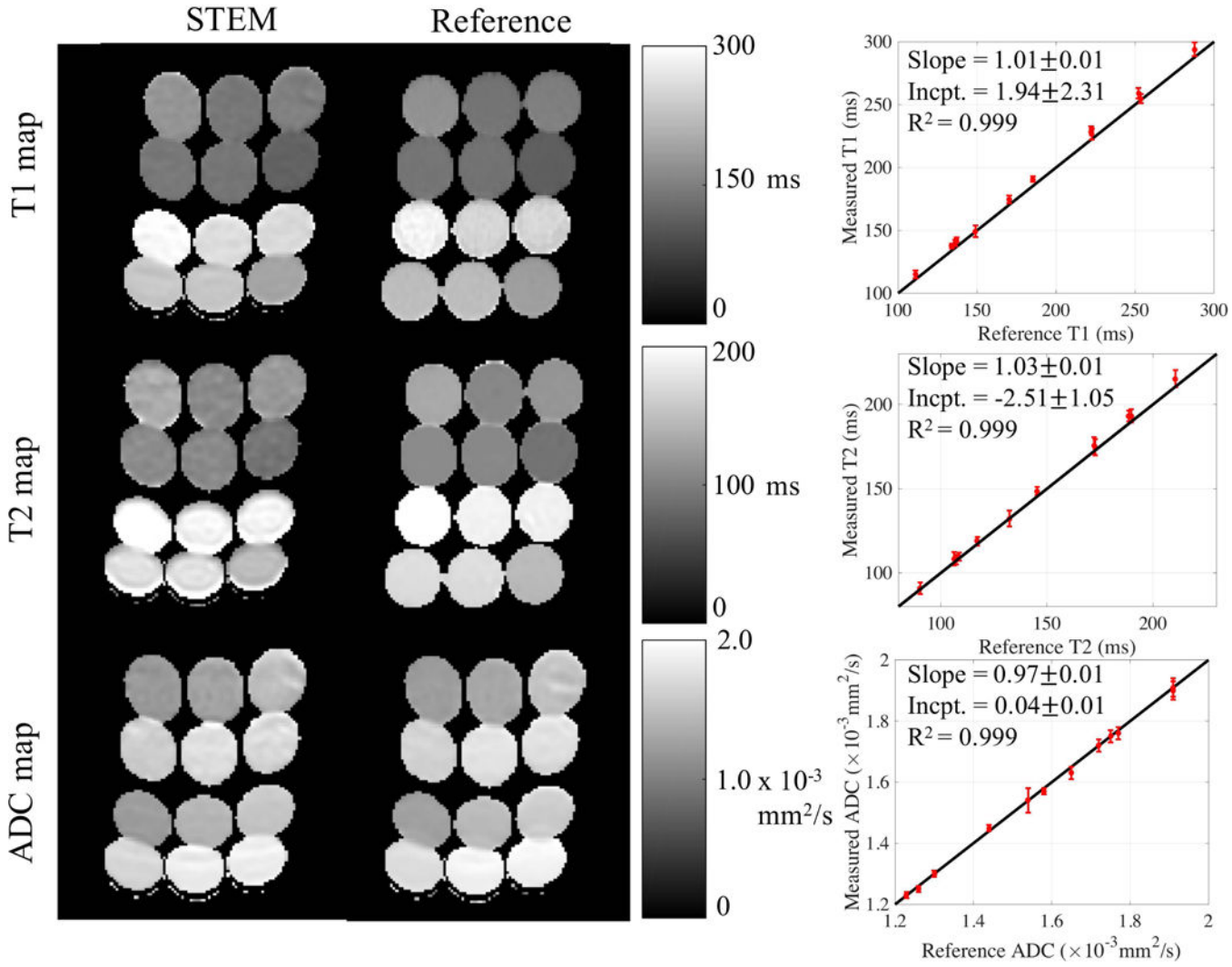

Figure 2.

T1, T2 and ADC maps estimated from STEM are accurate compared to the reference maps. The vials in the parametric maps have EPI distortion artifacts in the STEM images and the reference spin echo ADC map because of the EPI acquisitions. ROI measurements for each vial from STEM agree with the co-localized ROI results from the reference maps. The black lines in the plots to the right are the identity lines representing equal measurements and references.

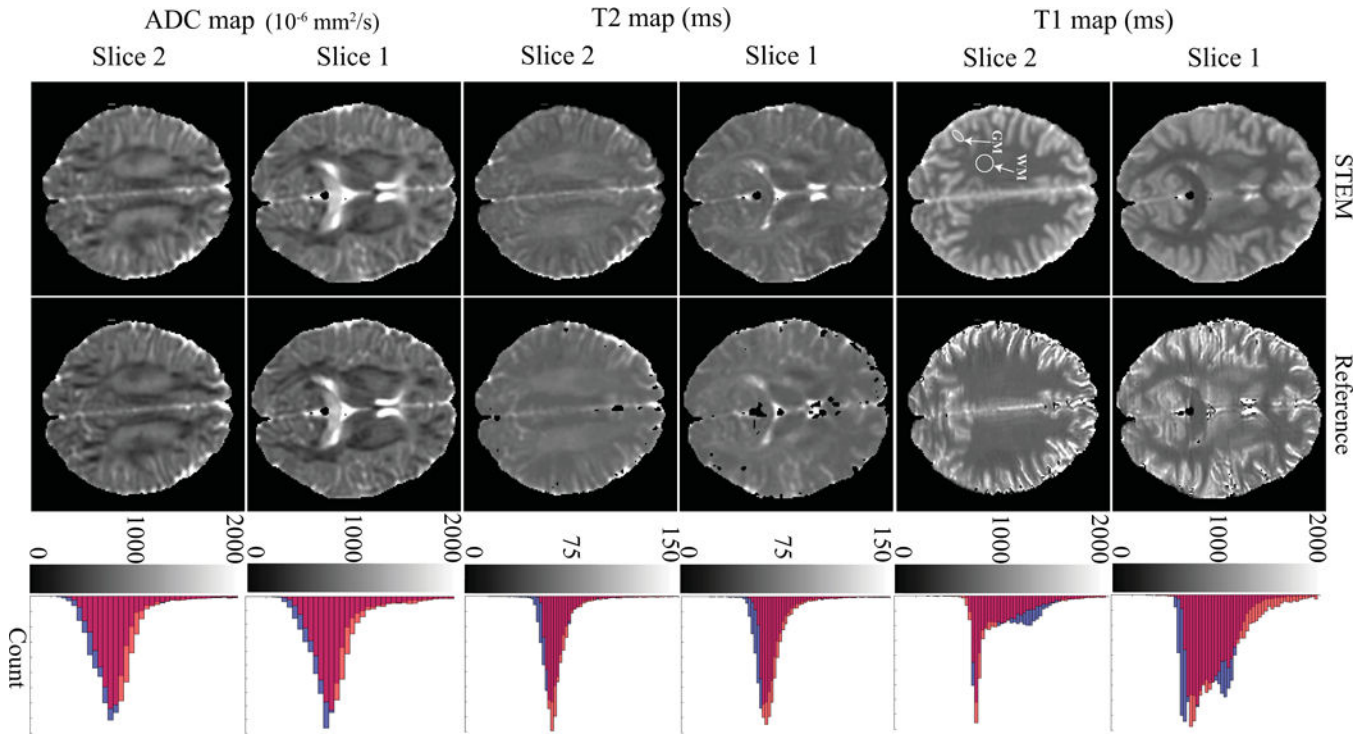

Figure 3.

The distributions of T1, T2 and ADC measurements in the brain from STEM are in good qualitative agreement with the reference measurements. The histograms to the right show the overall accuracy of each measurement from the entire slice. Orange bars in the histograms are from the reference maps, blue bars are measurements from STEM and the red color represents the overlapping area of reference and STEM-based histograms. The white arrows point to the ROIs in the white matter and gray matter.

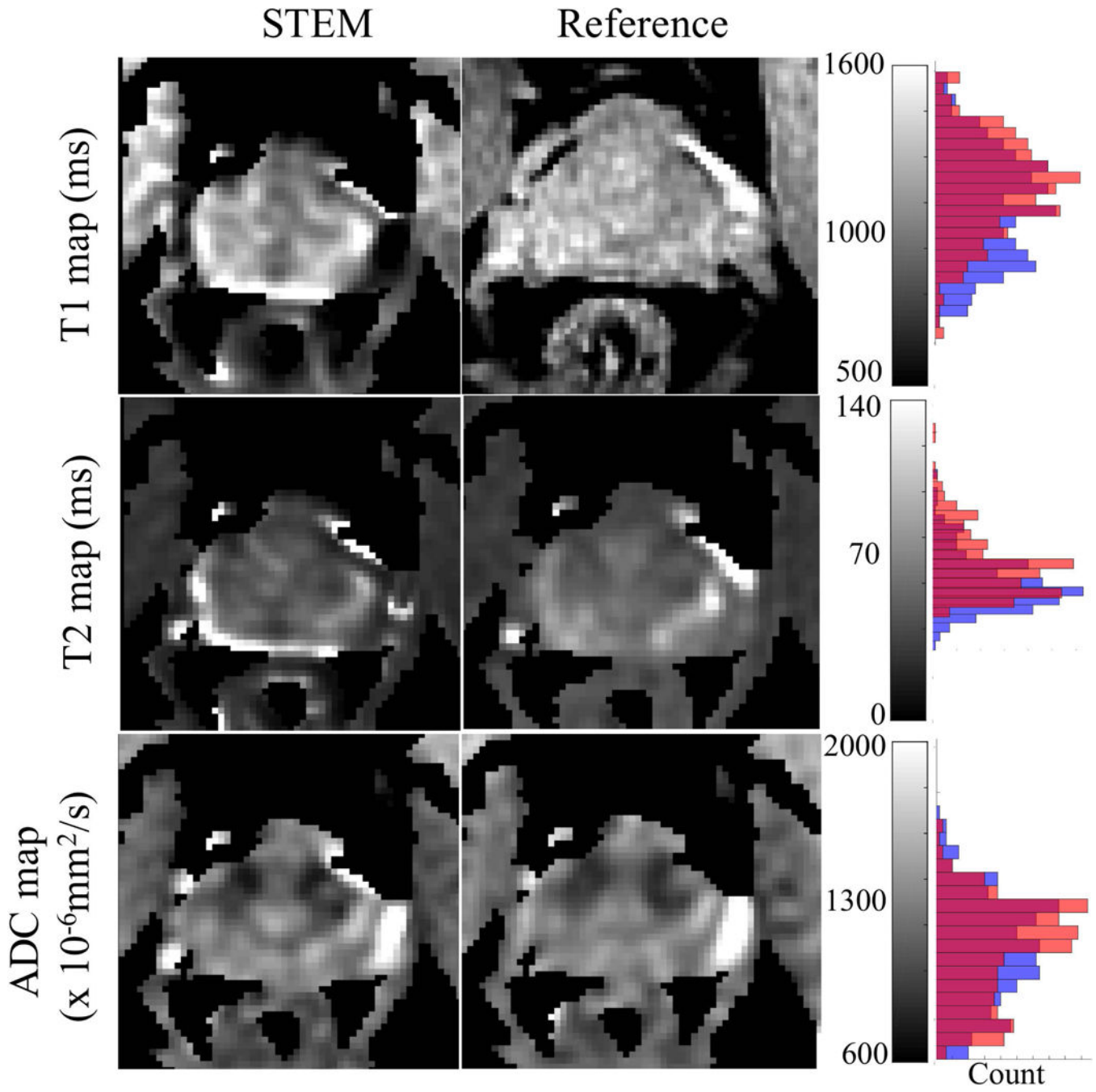

Figure 4.

The distributions of T1, T2 and ADC measurements in the prostate from STEM agree with the references, though with some bias in the T1 and T2 maps. Artifacts appearing at the edge of the prostate are mainly from the inter-acquisition motion from series to series. The histograms to the right show the overall accuracy of each measurement covering only the prostate area. Orange bars in the histograms are from the reference maps, blue bars are measurements from STEM and the red color represents the overlapping area of orange and blue bars.

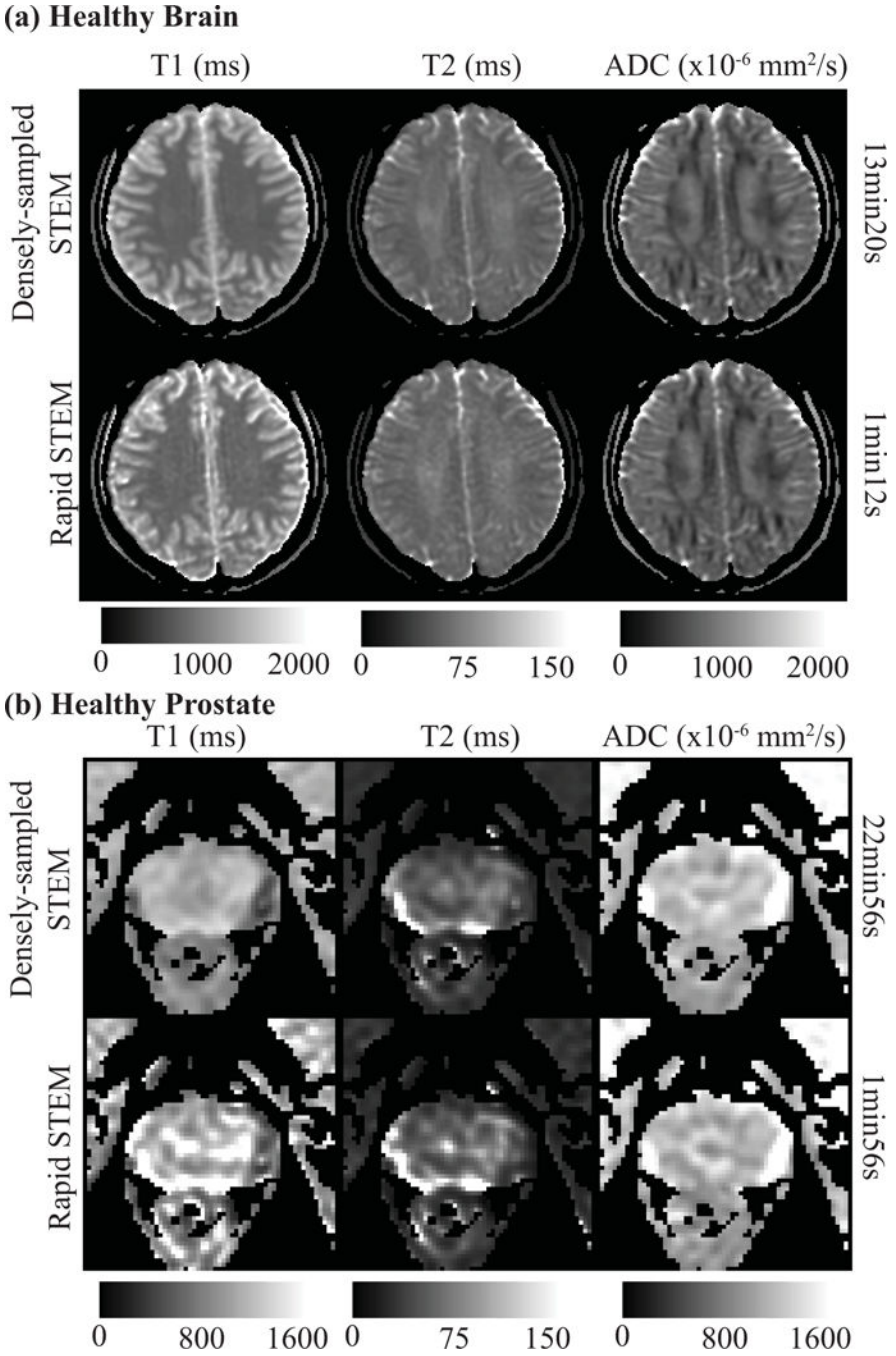

Figure 5.

An example of T1, T2 and ADC maps re-estimated retrospectively with the optimized rapid acquisition protocol (rapid STEM) are shown for healthy brain (a) and healthy prostate (b). The overall measurements are accurate even though the maps are noisier. The T1 map of healthy prostate shows some artifacts, likely due to motion without antiperistatic agents.

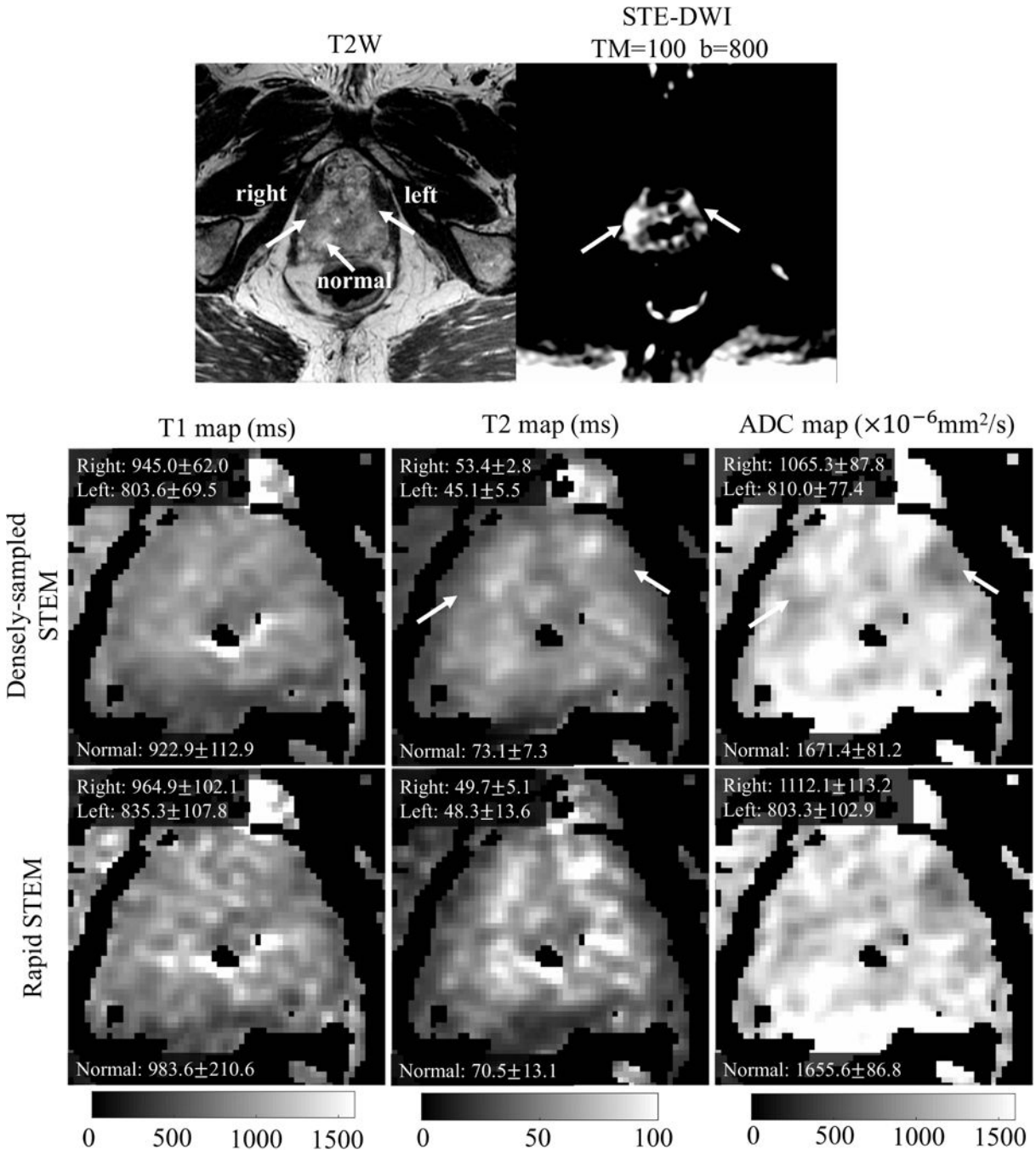

Figure 6.

The T2-weighted and DW images show the two cancerous lesions in the PCa patient. T1, T2 and ADC maps and ROI measurements of left PZ lesion, right PZ lesion and normal PZ tissue from the densely-sampled and the rapid STEM acquisitions are also shown.

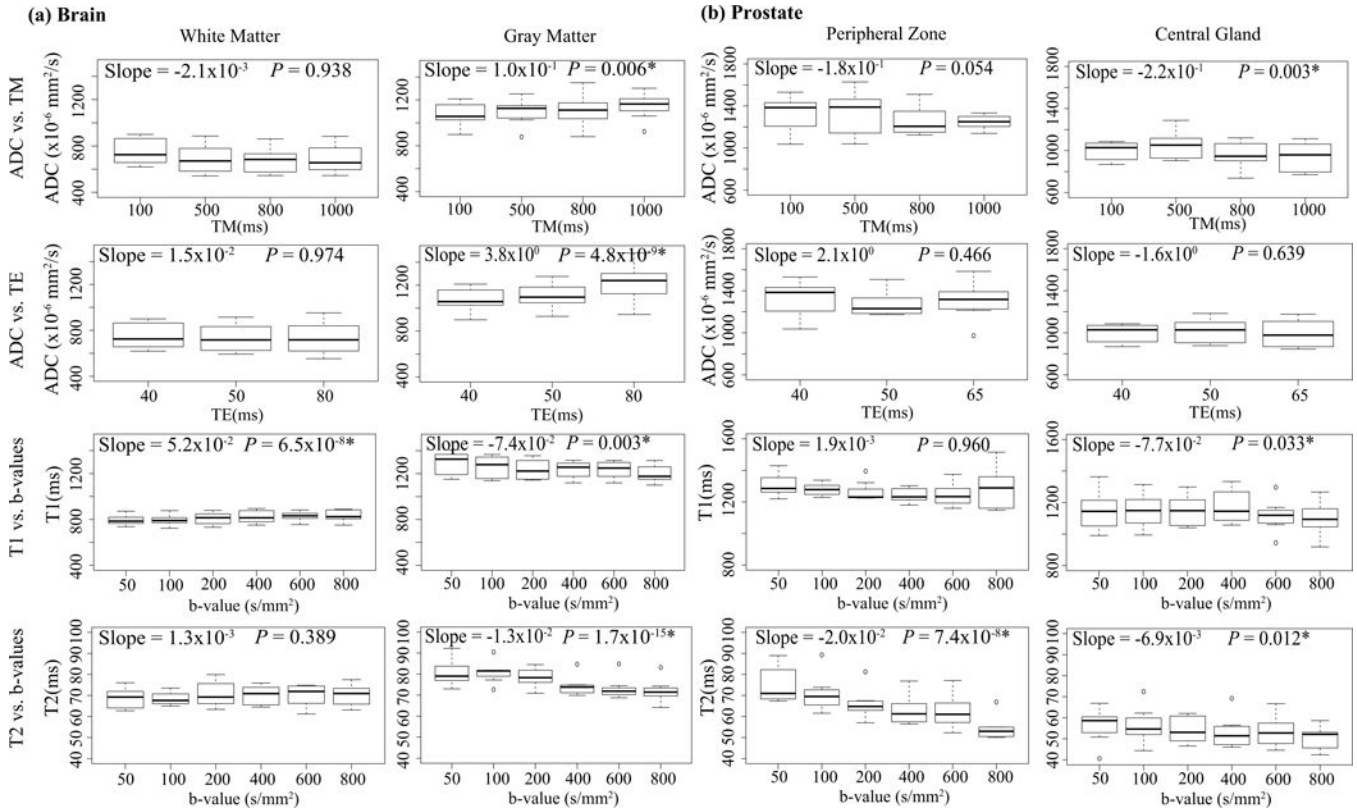

Figure 7.

Box-plots from ROIs measurements in the maps of each controlled group are shown for brain and prostate tissues, respectively. The linear mixed effect analysis results, including the slope and *P*-values, are labeled in each Box-plot.

Table 1

Phantom imaging protocol

IR FSE (Reference T1 mapping) (15min24s)	FOV = 28cm × 28cm, In-plane resolution = 1.1mm × 1.75 mm Slice thickness = 6mm, Average = 1, Bandwidth = ±15.63kHz, TR=6s TI = [50, 60, 70, 80, 90, 100, 110, 120, 130, 140, 150, 160, 170, 180] ms	
Multi-TE SE (Reference T2 mapping) (18min18s)	FOV = 28cm × 28cm, In-plane resolution = 2.2mm × 2.2 mm Parallel imaging factor = 2, Slice thickness = 6mm, Bandwidth = ±62.5kHz, TR=2s TE = [20, 40, 60, 80, 100, 140, 160, 180, 200] ms	
SE-DWI (Reference ADC mapping) (2min02s)	FOV = 28cm × 28cm, In-plane resolution = 2.2mm × 2.2 mm Parallel imaging factor = 2, Slice thickness = 6mm, Bandwidth = ±62.5kHz, TR=2s, Diffusion direction = three orthogonal diffusion directions (x, y, and z), b = [20, 50, 100(2), 300(4), 500(6), 800(6)] s/mm^2	
STEM (8min08s)	TM = 25ms, TE = 49.04ms	FOV = 28cm × 28cm, In-plane resolution = 2.2mm × 2.2 mm Parallel imaging factor = 2, Slice thickness = 6mm, Bandwidth = ±62.5kHz, TR=2s Same diffusion directions and b-values as SE-DWI
	TM = 100ms, TE = 39.84ms	
	TM = 100ms, TE = 100ms	
	TM = 200ms, TE = 36.34ms	

Table 2

In-vivo imaging protocol

(a) Brain Imaging		
IR FSE (Reference T1 mapping) (8min48s)	FOV = 28cm × 28cm, In-plane resolution = 1.1mm × 1.75 mm Slice thickness = 5mm, Average = 1, Bandwidth = ±15.63kHz, TR=6s TI = [50, 200, 350, 425, 500, 750, 900, 1100] ms	
Multi-TE SE (Reference T2 mapping) (10min10s)	FOV = 28cm × 28cm, In-plane resolution = 2.2mm × 2.2 mm Parallel imaging factor = 2, Slice thickness = 5mm, Bandwidth = ±62.5kHz, TR=1.8s TE = [30, 60, 90, 120, 150] ms	
STE-DWI (Reference ADC mapping) (1min40s)	FOV = 28cm × 28cm, Resolution = 2.2mm × 2.2 mm, Parallel imaging factor = 2, Slice thickness = 5mm, Bandwidth = ±62.5kHz, TR=4s, Diffusion direction = R/L, TM=100ms, TE =40ms, b== [50, 100, 200(2), 400(4), 600(6), 800(8)] s/mm^2	
STEM (13min20s)	TM = 25ms, TE = 49ms	FOV = 28cm × 28cm, Resolution = 2.2mm × 2.2 mm Parallel imaging factor = 2, Slice thickness = 5mm, Bandwidth = ±62.5kHz, TR=4s Diffusion direction = R/L, Same b-values as STE-DWI
	TM = 100ms, TE = 40ms	
	TM = 100ms, TE = 50ms	
	TM = 100ms, TE = 80ms	
	TM = 500ms, TE = 40ms	
	TM = 500ms, TE = 50ms	
	TM = 500ms, TE = 80ms	
	TM = 1000ms, TE = 40ms	

(b) Prostate Imaging		
DESPOT1 with B1 correction (Reference T1 mapping) (4min36s)	FOV = 28cm×28×14cm, In-plane resolution = 0.8mm × 0.57 mm Slice thickness = 5mm, Average = 4, Bandwidth = ±62.5kHz, TR=4s Flip angle = [10°, 5°, 1.8°]	
Multi-TE SE (Reference T2 mapping) (8min08s)	FOV = 26cm × 32cm, In-plane resolution = 2.5mm × 2.5 mm Parallel imaging factor = 2, Slice thickness = 5mm, Bandwidth = ±62.5kHz, TR=1.8s TE = [20, 60, 80, 120] ms	
STE-DWI (Reference ADC mapping) (2min52s)	FOV = 32cm × 32cm, Resolution = 2.5mm × 2.5 mm, Parallel imaging factor = 2, Slice thickness = 5mm, Bandwidth = ±62.5kHz, TR=4s, Diffusion direction = R/L, TM=100ms, TE =40ms, b= [50, 100, 200(2), 400(4), 600(6), 800(8)] s/mm^2	
STEM (22min56s)	TM = 25ms, TE = 49ms	FOV = 32cm × 32cm, Resolution = 2.5mm × 2.5 mm Parallel imaging factor = 2, Slice thickness = 5mm, Bandwidth = ±62.5kHz, TR=4s Diffusion direction = R/L
	TM = 100ms, TE = 40ms	
	TM = 100ms, TE = 50ms	
	TM = 100ms, TE = 65ms	
	TM = 500ms, TE = 40ms	
	TM = 500ms, TE = 50ms	
	TM = 500ms, TE = 65ms	
	TM = 1000ms, TE = 40ms	

Table 3

In-vivo ROI measurements

Brain	White matter			Gray matter		
	STEM	**Rapid STEM**	**Reference**	**STEM**	**Rapid STEM**	**Reference**
T1 (ms)	7 80.8 ±47.5	805.8 ±52.1	788.5 ±49.3	1241.4 ±119.1	1253.3 ±106.6	1219.9 ±92.3
T2 (ms)	65.6 ±4.2	67.5 ±4.9	67.1 ±4.0	71.4 ±6.4	77.5 ±8.1	76.9 ±6.2
ADC ($\times 10^{-6}$ mm^2/s)	6 90.7 ±125.4	708.0 ±120.9	710.0 ±126.9	9 28.6 ± 103.8	918.5 ±81.2	918.8 ±86.4
Prostate	Peripheral zone (PZ)			Central gland (CG)		
	STEM	Rapid STEM	Reference	STEM	Rapid STEM	Reference
T1 (ms)	1344.1 ±63.5	1420.4 ±217.2	1349.8 ±149.2	1156.7 ±65.6	1216.6 ±113.5	1244.5 ±104.3
T2 (ms)	65.1 ±6.3	68.1 ±10.3	7 0.6 ± 5.5	53.2 ±6.7	58.1 ±13.2	57.4 ±4.6
ADC ($\times 10^{-6}$ mm^2/s)	1200.7 ±102.4	1151.5 ±141.4	1 140.9 ±132.2	1038.0 ±88.8	1040.2 ±136.4	1038.1 ±97.2